International Journal of Heat and Mass Transfer 225 (2024) 125407

Contents lists available at ScienceDirect

International Journal of Heat and Mass Transfer

journal homepage: www.elsevier.com/locate/ijhmt

Investigating the stability mechanisms of single bulk Nanobubbles: A molecular dynamics perspective

Jiajie Lei [a], Dezhao Huang [a,*], Wensheng Zhao [a], Sheng Liu [b,*], Yanan Yue [a,*]

[a] School of Power and Mechanical Engineering, Wuhan University, Wuhan, Hubei 430072, PR China
[b] The Institute of Technological Sciences, Wuhan University, Wuhan, Hubei 430072, PR China

ARTICLE INFO

Keywords:
Nanobubbles
Molecular dynamics
Thermodynamic stability
Bubble dynamics

ABSTRACT

In this study, we investigated the relationship between bubble stability and various parameters, including radial pressure, density, surface tension, charge distribution, and Brownian motion, using molecular dynamics simulations and classical bubble stability theory. Our research sheds light on the contrasting behavior of small and large nanobubbles in water, with larger bubbles demonstrating a prolonged lifespan and lower internal pressure. Specifically, nanobubbles with radii of 14 Å, 18 Å, and 22 Å were found to have pressures of 792 atm, 647 atm, and 518 atm, respectively. Notably, our calculations revealed that smaller bubbles possess a thicker liquid-gas interface compared to the larger bubbles. Additionally, our analysis of gas-liquid interactions and mean squared displacement demonstrated that smaller bubble gas molecules experience stronger liquid forces and exhibit enhanced diffusivity. Importantly, we validated the reliability of classical theories by confirming the consistency between the calculated solubility of nanobubbles using Henry's law and simulation results. Moreover, our findings aligned with the predictions of Young's equation regarding surface tension at the calculated plane, highlighting its applicability in understanding nanobubbles behavior. Notably, we observed that gas density has minimal impact on the surface tension of nanobubbles according to Young's equation. Overall, our research provides valuable insights into the generation of stable nanobubbles for diverse applications.

1. Introduction

Nanobubbles are defined as bubbles with a volume-equivalent diameter of less than 1 μm according to ISO 20,480–1:2017 [1]. Nanobubbles have become a versatile tool with a wide range of applications, including precision diagnostics [2–4] and environmental remediation [5,6]. In the realm of medicine, the utilization of laser-induced vapor nanobubbles on nanoparticle surfaces has revolutionized the attainment of precise transport mechanisms for cancer treatment [7,8]. Simultaneously, the surface structures within microdevice heat transfer systems, characterized by their roughness [9] and hydrophobic nature, have been revealed as influential factors in the stabilization [10,11] and heightened nucleation efficiency of nanobubbles. Moreover, the generation of nanobubbles can be indirectly achieved [12] during laser fabrication processes [13,14] and the preparation of two-dimensional materials [15–17]. Recent investigations have delved into the intricate behavior and properties of nanobubbles across diverse processes, while compelling experimental evidence [18] has also substantiated their remarkable stability in the medium, persisting over extended periods even after dissolution.

Compared to microbubbles, nanobubbles possess a unique characteristic of low buoyancy, which effectively prevents their buoyant rise and subsequent breakup upon contact with water. Nanobubbles can be classified into two distinct types based on their mode of existence: surface nanobubbles [19] and bulk nanobubbles. The kinetic evolution of surface nanobubbles adheres to the principles of the diffusion equation, the Laplace equation, and Henry's law. In particular, stable surface nanobubbles can be obtained when gas flows in from gas-supersaturated water and out due to Laplace pressure equilibrium [19]. Lohse et al. have demonstrated through experiments [20] and molecular dynamics simulations [21] that the immobilization of three-phase contact lines at chemical or geometric surface heterogeneities is the primary factor contributing to the extended lifetime of surface nanobubbles. However, the stability of bulk nanobubbles remains a subject of ongoing scientific discourse, warranting further investigation. Various indirect imaging and characterization techniques, such as dynamic scattering techniques [22], zeta potential shift [23], and cryoelectron microscopy [24], have been employed to probe the properties of bulk nanobubbles [18].

* Corresponding authors.
E-mail addresses: dhuang2@whu.edu.cn (D. Huang), victor_liu63@vip.126.com (S. Liu), yyue@whu.edu.cn (Y. Yue).

https://doi.org/10.1016/j.ijheatmasstransfer.2024.125407
Received 12 January 2024; Received in revised form 21 February 2024; Accepted 4 March 2024
Available online 10 March 2024

However, direct evidence supporting their ultra-long stability remains elusive. The presence of contaminants during experimental procedures has significantly interfered with the accurate detection and characterization of nanobubbles [22]. A recent study by Kim and Najafi et al. [25] utilized ultrasound and heating to generate bulk nanobubbles and observed a consistent zeta potential measurement on the nanoparticles, aligning with that of larger bubbles. This study underscores the critical importance of meticulous experimental design and rigorous control of contaminant presence to ensure precise detection and characterization of nanobubbles.

The stability mechanisms of bubbles have sparked theoretical debates in the field. Currently, four mechanisms have been proposed: the contaminant mechanism, epidermal mechanism, surface zeta potential mechanism, and high internal gas density mechanism [26,27]. However, experimental evidence has raised questions regarding the validity of some of these mechanisms. For example, Ghaani et al. [28]. utilized surface electrostatics to generate bulk nanobubbles and discovered that the stability of these bubbles stems from surface polarization, which is independent of the bubble charge. Additionally, the properties exhibited by nanobubbles challenge classical theory [22], which predicts high internal pressure and short lifetimes for such bubbles. Nevertheless, experimental observations have demonstrated the remarkable persistence of nanobubbles over extended periods, casting doubt on the applicability [29,30] of Young's Laplace equation for nanobubbles.

Despite extensive research, the understanding of the fundamental properties of bulk nanobubbles remains highly controversial. To contribute to this ongoing discussion, we conducted a series of molecular dynamics simulations to investigate the intricate processes of formation, dissolution, and stabilization of individual nanobubbles. Our study highlights the critical role of achieving thermodynamic equilibrium between the nanobubbles and the surrounding liquid, which is essential for efficient gas diffusion within the nanobubbles structure. To assess the influence of nanobubbles size on stability, we meticulously analyzed radial density, pressure, and charge distributions. Furthermore, we rigorously compared our numerical results with established classical theories, including Young's Laplace equation, Epstein and Plesset's lifetime prediction theory, and Henry's law, confirming their applicability and validity in the realm of nanobubbles. In addition to fundamental investigations, we also explored the practical implications of nanobubbles in various industrial applications by investigating their mean squared displacement and Brownian motion. Our comprehensive study not only advances the understanding of the underlying mechanisms that govern the stability of bulk nanobubbles but also provides valuable insights for potential applications in heat and mass transfer.

2. Physical model and methods

To investigate the nanobubbles properties and analyze the mechanism, molecular dynamics simulations were performed using the classical MD code-Large-scale Atomic/Molecular Massively Parallel Simulator (LAMMPS) [31]. The simulation system is visualized using the open visualization tool-OVITO [32] during the simulation. We use a cluster of nitrogen molecules [33–35] to represent our nanobubbles since it constitutes a major part of the gaseous nanobubbles. To accurately calculate the nanobubbles properties, the SPC/E water model was used since it can match well with the experimental results in calculating the density, diffusion coefficient, and viscosity of water. [36–38] In the simulation, the interaction forces between nitrogen and nitrogen/water molecules are described by the Lennard–Jones (L-J) potential, formulated as:

$$\phi(r_{ij}) = 4\varepsilon_{ij}\left[\left(\frac{\sigma_{ij}}{r_{ij}}\right)^{12} - \left(\frac{\sigma_{ij}}{r_{ij}}\right)^{6}\right]_{r<r_c} \quad (1)$$

where ε is the energy parameter, σ is the length parameter and r_c is the cut-off radius. The cut-off radius between water molecules and nitrogen/water molecules is set to 10 Å. Long-range Coulomb interactions are calculated by the particle- particle-mesh (PPPM) solver [39]. The potential parameters between the atoms are shown in Table S1, where q is the atomic charged charge. Periodic conditions are used for all boundaries. The chosen size of the time step is 1 fs. The simulation model is a cube of length $L = 80$ Å, mainly divided into water and gas regions, where the gas region is located in the center of the system with a radius of 20 Å (see Figure S1). Nanobubbles with three different sizes containing different gas molecules (small: 206 N_2 molecules, medium: 301 N_2 molecules and large: 409 N_2 molecules) were built to study the effect of the gas molecule content on the solubility, stability, and Brownian motion of the nanobubbles. All nanobubbles are immersed in the liquid environment which consists of 15,249 water molecules.

A four-stage MD simulation study was conducted to investigate the dissolution, stability, and motion properties of bubbles. Initially, the system was simulated in canonical ensemble (NVT) for 2 ns, with a controlled temperature of 300 K, and the gas confined to the initial bubble. Subsequently, the isothermal-isobaric ensemble (NPT) was employed to remove the spatial constraints of the bubbles while maintaining a constant pressure of 1 atm and a temperature of 300 K. During the NPT simulation, the dissolution properties of the bubble were analyzed by counting the number of gas molecules inside and dissolved into the water to determine the thermodynamic stability of the nanobubbles. The NPT simulation was terminated when the bubble reached thermodynamic stability, which was determined based on the number of gases inside and outside the bubble. During the simulation, when the bubble reached thermodynamic stability, the properties were analyzed in the microcanonical ensemble (NVE) for 2 ns. This is because for liquid systems the NVE ensemble is the optimal ensemble for statistical system properties and the thermostats/pressures of the other ensembles interfere with the dynamics of the system [40]. It is difficult to count the thermophysical properties at equilibrium because the nanobubbles will undergo Brownian motion during the simulation. The mass center of the bubble is controlled in the current simulation by reference to Thompson et al. [41]. The simulation results are unaffected by atomic coordinate translations due to the use of periodic conditions [33]. To account for thermal fluctuations, the bubbles were not perfect spheres in any ensemble, but were considered spheres for statistical analysis if the nanobubbles equilibrium time was long enough. In the all-atom model, based on the geometric clustering criterion [42,43], two gas molecules within a nanobubble are considered to be clustered when their distance is less than 5 Å [33]. Therefore, the spherical shell positions 6 Å to 39 Å were selected for thermodynamic radial distribution statistics, considering the effects of the number of statistical atoms and periodic boundaries. Finally, the restriction of the bubble's fixed center-of-mass was lifted to study its Brownian motion properties at NVE (2 ns) conditions.

3. Results and discussion

3.1. Lifespan and dissolution

The stability of nanobubbles is achieved after a period of dissolution subsequent to their generation, which is challenging to measure experimentally due to the dynamic behavior of these bubbles. To investigate the dissolution mechanism, a dynamic statistical region with a 20 Å radius is established, and the number of atoms enclosed within the nanobubbles is statistically sampled using NPT ensemble simulations (Fig. 1). In Fig. 1a-c, it is evident that the smaller nanobubbles experience a rapid contraction phase before reaching a stabilized state, resulting in a significantly smaller size compared to their initial size. Conversely, medium-sized nanobubbles (Fig. 1d-f) exhibit relatively stable sizes throughout the dissolution process. Due to the use of fixed regions filled with atoms for nanobubble construction, large-sized nanobubbles (Fig. 1g-i) undergo an expansion of a few femtoseconds during the ensemble transition (the system is unstable) and then begin to

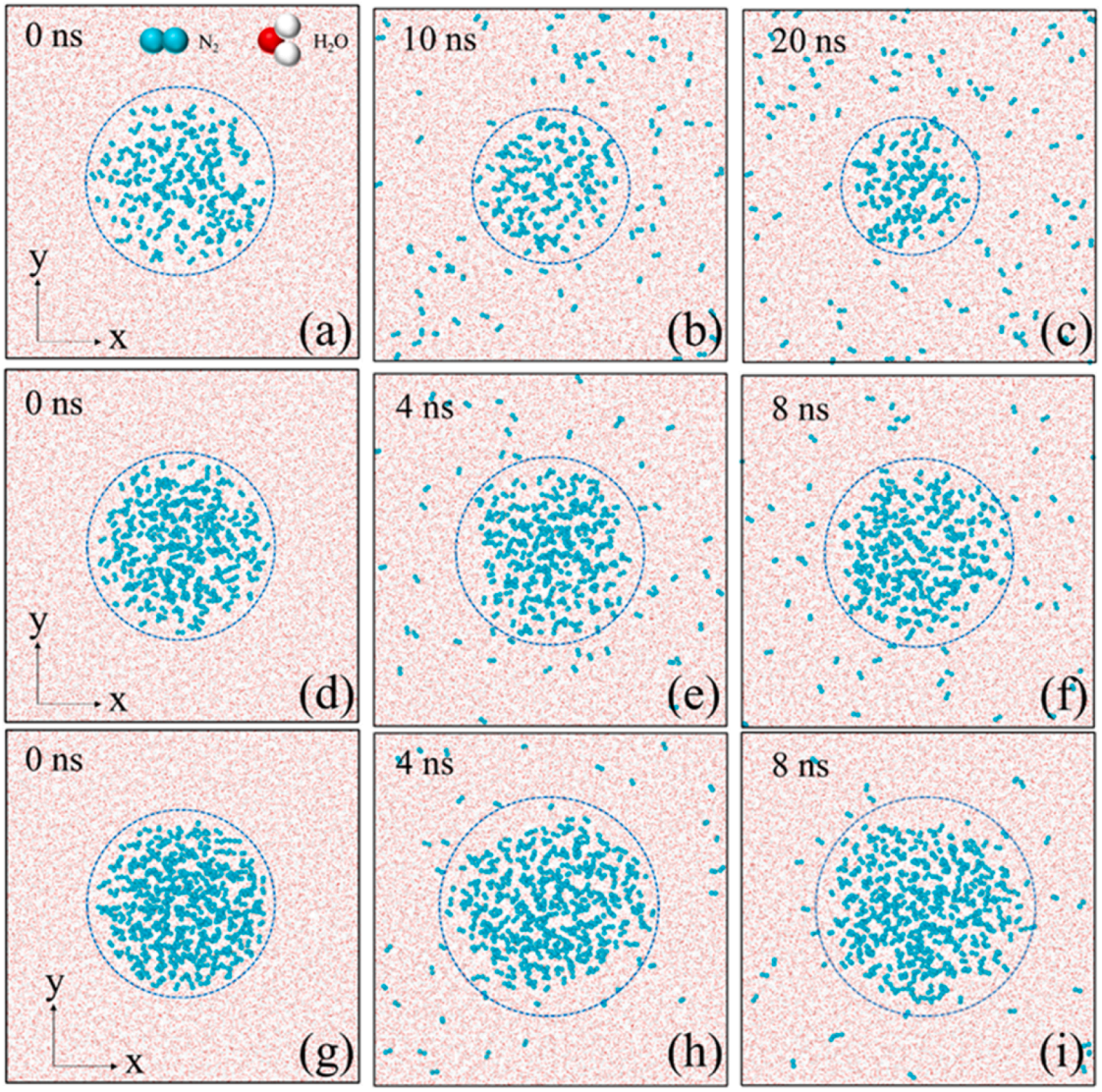

Fig. 1. Temporal progression of nanobubbles categorized as small (a-c), medium (d-f), and large (g-i) during the process of dissolution. The blue circle represents the actual nanobubbles region throughout the dissolution, accounting for the fluctuation in size. Oxygen and hydrogen atoms in water molecules are denoted by red and white points, respectively, whereas cyan points signify nitrogen atoms in nitrogen gas molecules.

contract. Note that this expansion of the bubble does not compromise the validity of the subsequent statistical findings presented in our study. These artefacts, manifesting transiently during the ensemble transition phase for mere femtoseconds, were consequently excluded from our data analysis. Our analysis of nanobubble dynamics during the dissolution process employed the NPT ensemble, ensuring each model underwent a minimum simulation duration time of 10 nanoseconds. This long simulation time has already effectively mitigated any artefact-related influences in the previous transition processes. For the larger nanobubbles, the size exceeds the statistical region (20 Å) due to molecular dynamics artefacts at the system transition. Hence, we expanded the statistical region to 23 Å at 5 ns (Fig. 2d). Additional details regarding the change in the approximate radius and the statistical region for different bubble sizes are provided in the Supplementary Information (as shown in Figure S2). By analyzing the temporal changes in the number of bubble atoms within the statistical region, we observe that smaller nanobubbles undergo a contraction phase lasting 20 ns before stabilizing (Fig. 2a). In contrast, medium-sized nanobubbles, as shown in Fig. 2b, maintain a relatively constant size and achieve stability within 5 ns. In the case of larger bubbles, stabilization is achieved prior to 5 ns (Fig. 2c). This observation indicates that the greater the number of atoms present within the bubble, the quicker the stabilization time is attained.

To analyze the dissolution process of the nanobubbles, we calculated the mean square displacement (MSD) of the gas molecules inside the nanobubbles. To avoid the artifacts associated with fixed bubbles, we lifted the bubble constraints and subtracted the bubble center-of-mass drift to calculate the MSD of the internal gas. The diffusion coefficient of the nanobubbles based on the MSD can be calculated as

$$D = \lim_{t\to\infty} \frac{\left\langle [r(t) - r(t_0)]^2 \right\rangle}{6t} \tag{2}$$

Where r(t) is the position vector of the atom at moment t and the average was over the time origin for the autocorrelation. The MSD results of nanobubbles containing 206, 301 and 409 gas molecules are shown in Fig. 3a. The diffusion coefficients of nanobubbles were calculated to be 2.57×10^{-9} m^2/s ($N = 206$), 1.29×10^{-9} m^2/s ($N = 301$) and 1.05×10^{-9} m^2/s ($N = 409$), respectively. The diffusion coefficient of molecules inside the $N = 206$ nanobubbles is nearly twice that of the $N = 409$ nanobubbles. Meanwhile, the solubility of the gas in the liquid can be obtained from the number of molecules of the dissolved gas (as shown in

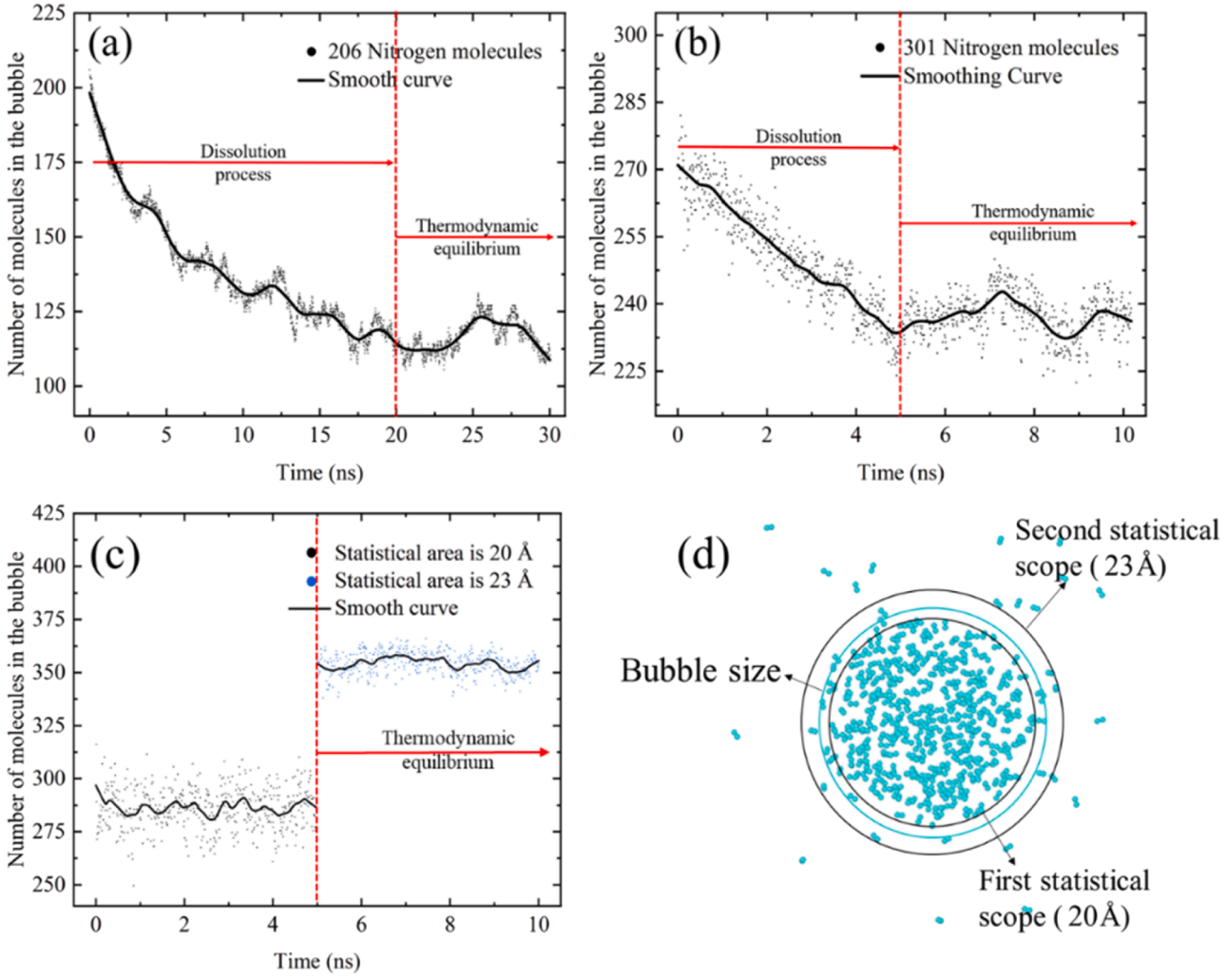

Fig. 2. Dissolution curves of the (a) small, (b) medium and (c) large nanobubble under NPT conditions. The bubbles undergo a dissolution process to reach a state of thermodynamic equilibrium. (d) The radius of the large bubble is wider than the initial statistical region due to the high number of atoms inside. To ensure accurate counting of the atoms inside the large bubble, we expand the counting area from 20 Å to 23 Å after 5 ns.

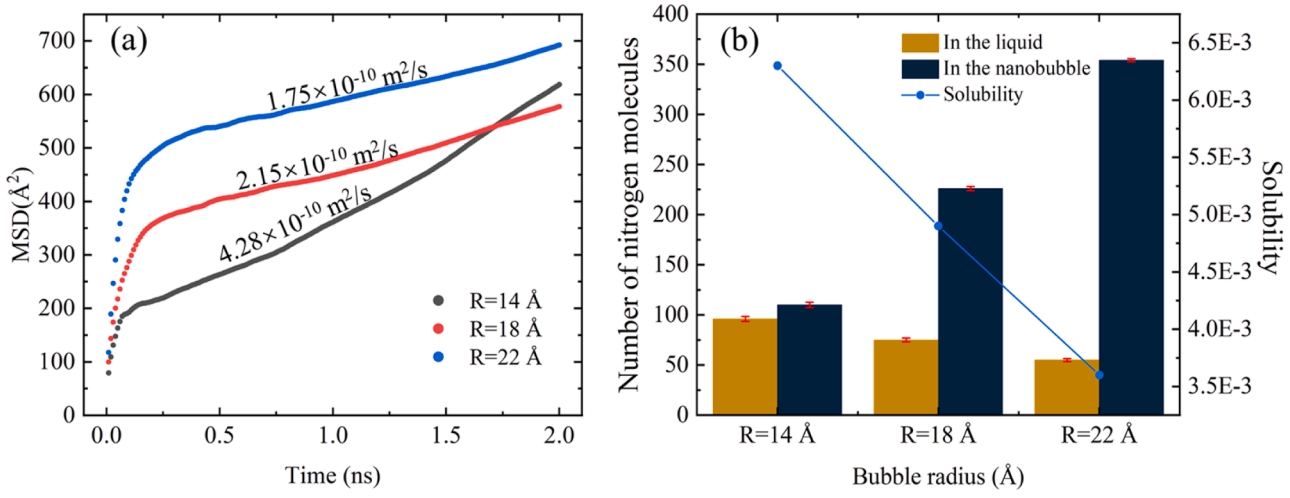

Fig. 3. (a) Investigation of gas molecule diffusion coefficients within nanobubbles is presented for NVE ensembles. The study examines the effect of gas molecule number (N) on diffusive behavior within nanobubbles by analyzing the slope of mean squared displacement (MSD) between 1 and 2 ns. (b) The equilibrium solubility of bubbles with varying radii is explored through an analysis of the ratio of dissolved gas content (orange bar) to the gas inside the bubble (dark blue bar). This ratio provides an estimate of bubble stability. The solubility is determined by the molar fraction of dissolved gas in relation to the molar fraction of water.

Fig. 3b). Theoretically, the dissolution of nitrogen at standard pressure (1 atm) and temperature (300 K) is 1.1×10^{-5} (molar fraction). However, in the present study, the solubility of nitrogen nanobubbles was much greater than the standard state and the liquid reached transitional saturation. In experimental studies, the lifetime of nanobubbles has been observed to be finite. However, molecular dynamics simulations are constrained by temporal limitations that preclude the observation of bubble disappearance. Employing the classical theory of bubble stability [44], we have computed the lifetime of nanobubbles of varying radii. Our calculations yield the estimated lifetimes of nanobubbles.

$$T_{\text{life}} \approx \frac{R^2 \rho_g}{3DC_s} \tag{3}$$

where ρ_g is the gas density inside the bubble, D is the diffusion coefficient of the gas in the liquid, C_s is the solubility of the gas. The findings demonstrate that bubbles with radii of 14 Å, 18 Å, and 22 Å have lifetimes of 28 ns, 104 ns, and 227 ns, respectively. Feng et al. have similarly predicted the lifetime of nanobubbles, which they suggest is also at the nanosecond level [45]. In contrast, the experimental data shows that nanobubbles can have lifetimes of hours or even days. Discrepancies between the theoretical and experimental results may stem from differences in bubble size and the bubble population effect. Hong et al. [46]. found that the spacing between bubble clusters also contributes to the stability of nanobubbles, and that the spacing is related to the radius of the nanobubbles. For systems with multiple nanobubbles, high supersaturation within the solution and dissolution of the neighboring nanobubbles inhibits the diffusion of gases from the nanobubbles into the surroundings [47].

3.2. Thermodynamic stabilization of nanobubbles

The long-term stability of nanobubbles has been a controversial topic, despite their initial rapid dissolution in aqueous solutions. This study aims to shed light on the mechanism behind their stability by exploring the state of nanobubbles at thermodynamic equilibrium. Through NVE ensemble simulations and statistical sampling of thermodynamic properties, we calculated the radial density distributions of the liquid and gas in order to determine the equilibrium radius of the nanobubbles. Our analysis revealed that the gas-liquid density distribution of the bubbles showed an absence of water molecules inside and that the liquid density away from the bubbles reached that of water at standard temperature and pressure as shown in Fig. 4a-c. However, obtaining the bubble equilibrium radius was challenging due to difficulties in maintaining a standard spherical shape during the simulation. To address this, we fitted the liquid-gas density using a hyperbolic

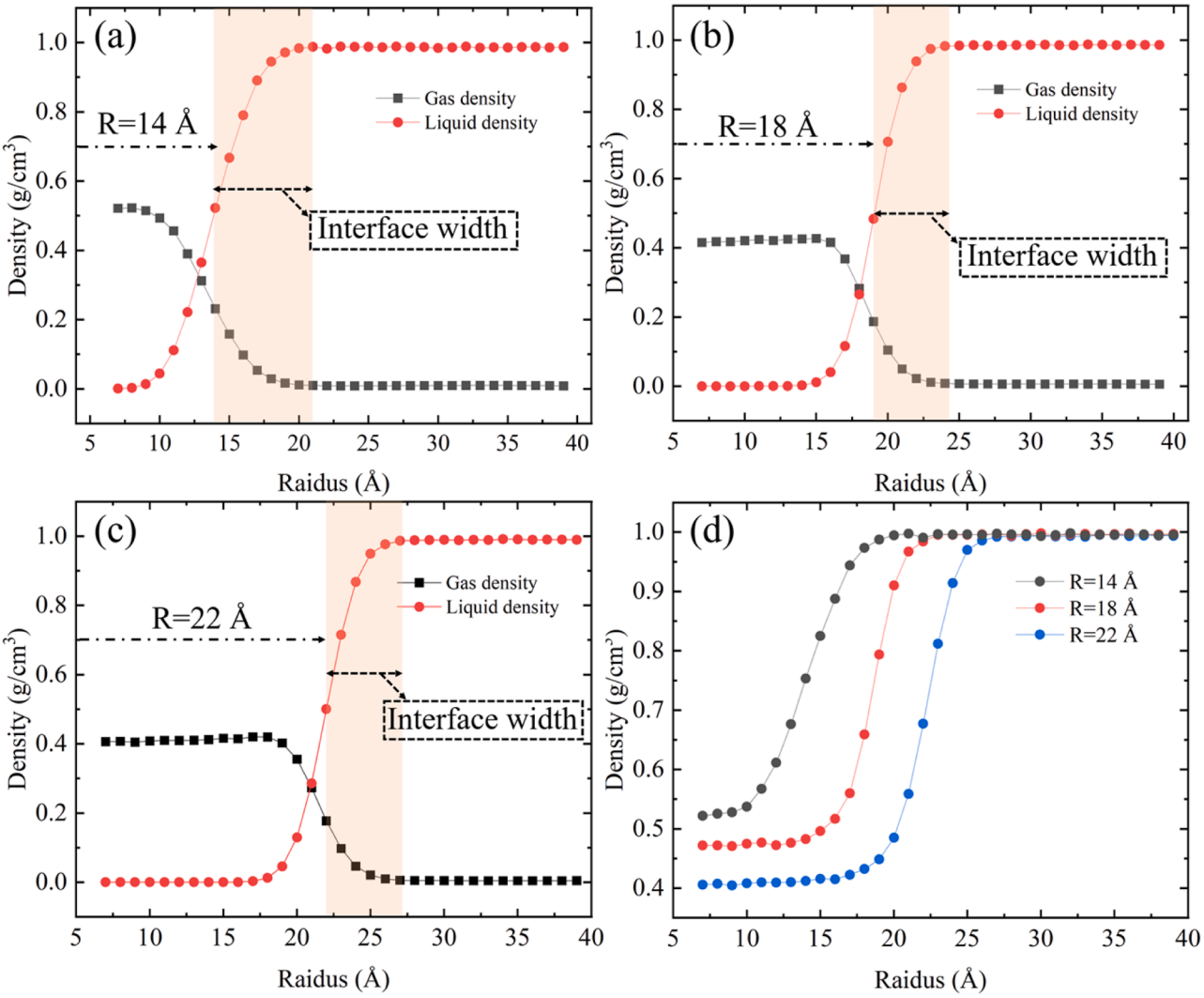

Fig. 4. Nanobubbles containing (a) 206 (R = 14 Å), (b) 300 (R = 18 Å), and (c) 400 (R = 22 Å) gas molecules show the radial density distribution and gas-liquid interface widths of the liquid and gas, respectively. The orange area is the width of the liquid-gas interface. The equilibrium radius of the nanobubbles was estimated by hyperbolic tangent fitting based on the (d) density distribution of the three different systems.

tangent function, which was found to be consistent with the observed radial density distribution [48].

$$\rho(r) = \frac{\rho_{in} + \rho_{out}}{2} - \frac{\rho_{in} - \rho_{out}}{2} \tanh(2(r - R_0) / \zeta) \quad (4)$$

Where ρ_{in} is the density inside the bubble, ρ_{out} is the density of the water, ξ is the liquid-gas interface width. Based on Eq. (4), we found that bubbles containing 206, 301, and 409 gas molecules reach thermodynamic equilibrium at radii of 14 Å, 18 Å, and 22 Å, respectively. Fig. 3d shows that small-sized nanobubbles have higher density. According to the ideal equation of state, the small bubbles should have a high pressure inside, which leads to a faster diffusion rate of the gas inside. Furthermore, we noted that the liquid-gas interface widths for the three cases were 6.8 Å (R = 14 Å), 5.6 Å (R = 18 Å), and 4.4 Å (R = 22 Å). The thickness of the liquid-gas interface layer increased as the size of the bubble decreased. This observed trend is consistent with the results measured experimentally by Zhang et al. [49]. Pan et al. used a molecular dynamics approach to study the effect of a periodically oscillating electric field on the interface between methane and water [50]. It was found that the thickness of the interface between methane and water increased with increasing frequency of the electric field and that the mass transfer between methane and water was enhanced, leading to further dissolution of methane. Therefore, we speculate that the nanobubble interfacial thickness similarly affects the diffusion of the gas inside the bubble. As the interfacial thickness increases, the contact area between the gas and water increases, thus leading to enhanced mass transfer of the gas.

3.3. Mechanically stable mechanisms

In the state of thermodynamic equilibrium, where a bubble is fully immersed in a surrounding liquid, it maintains mechanical equilibrium as well. This phenomenon is explained by Young's equation:

$$P_{in} = P_{out} + \frac{2\gamma}{R_0} \quad (5)$$

where, P_{in} is the internal pressure of the nanobubble, P_{out} is the outside pressure of the nanobubble, γ is the surface tension at the liquid-gas interface at the nanobubble boundary, R_0 is the bubble equilibrium radius. We calculated the pressure distribution of the system along the radial direction using the Harasima method [51], and detailed equations are given in the Supplementary Information. Fig. 4 shows the radial distribution of pressure in the system, which is consistent with the theoretical framework of Young's equation. The results indicate that smaller bubbles exhibit higher pressures. Specifically, the R = 14 Å nanobubble displayed a remarkably high pressure of 792 atm, which was 1.5 times greater than that of R = 22 Å. Notably, the liquid-gas interface was found to exhibit a strong negative pressure, particularly in the case of the R = 22 Å bubble. The observed negative pressure at the gas-liquid interface may contribute to maintaining the mechanical equilibrium of the bubbles. Moreover, we have observed that the liquid pressure surrounding the bubbles consistently maintains an average of 1 atm, and this observation is further supported by the confirmed density distribution (Fig. 4d).

The negative pressure in the liquid is primarily attributed to the presence of surface tension at the interface between the two phases. This surface tension causes the liquid atoms at the interface to undergo stretching, leading to the generation of negative stress. In the Supplementary Information (Figure S3), we have included the radial pressure distribution of the liquid atoms. It is evident from the data that the negative pressure of the liquid surrounding the bubble remains consistent across different radii. Young's equation can calculate the surface tension at the gas-liquid interface by analyzing the pressure inside the nanobubbles as seen in Fig. 5a. In this study, we constructed a simple planar model representing the liquid-gas boundary, considering different gas densities that align with those in bubbles (refer to Supplementary Information for more information). This model was then used to validate the predictions made by Young's equation, as detailed in Table 1. Our findings indicate that the surface tension values (γw) calculated using Young's equation, which are based on liquid pressure, align closely with those obtained from our model. This consistency confirms the applicability of Young's equation at the nanoscale. Moreover, our analysis of nanobubbles of different sizes demonstrates that the internal gas density has minimal impact on the surface tension at the liquid-gas interface. This observation is consistent with the results

Table 1
Surface tension at the gas-liquid interface of different bubbles.

Bubble radius	R = 14 Å	R = 18 Å	R = 22 Å
γ_w (mN/m)	55.35	57.95	56.83
γ_m (mN/m)	56.49	58.29	58.43

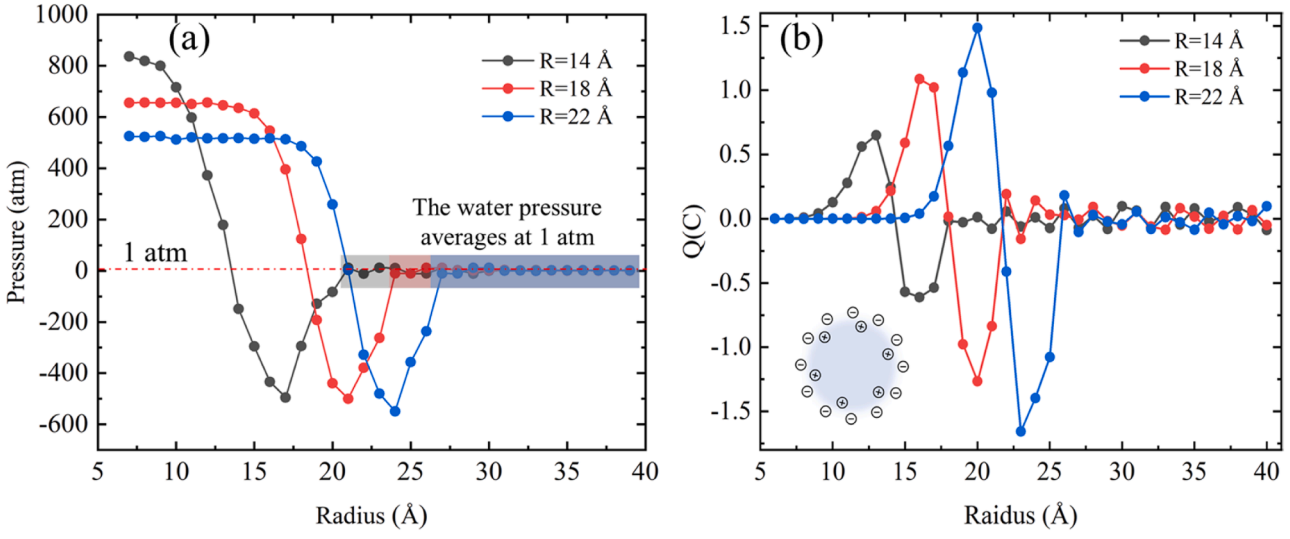

Fig. 5. (a) Radial pressure distribution of the system. In the homogeneous region, the pressure inside and outside the bubble is expressed as $P = (P_{xx}+P_{yy}+P_{zz})/3$. The pressure of the liquid surrounding the bubble averaged 1 atm. (b) Radial distribution of charges around the bubble. The bubble is surrounded by a double layer of electrostatic charge distributions. The inner layer is being positively charged and the outer layer is negatively charged.

obtained from the analysis of the radial pressure distribution of the liquid, which further confirms that the negative pressure observed at the liquid-gas interface is indeed a direct result of the surface tension. It is worth noting that our findings are consistent with insights gained from investigations into surface bubbles [52]. Teshima [53] used molecular dynamics to observe a phenomenon consistent with Atomic Force Microscopy (AFM), where the internal gas density has little effect on the surface tension of the surface nanobubbles.

The stability of nanobubbles is influenced by various factors, including electrostatic repulsion. The experimental results demonstrate that nanobubbles possess a highly negative surface charge, as indicated by the zeta potential measurements. To gain insight into the underlying mechanism responsible for bubble stability, we examined the radial distribution of charge around the bubble, as depicted in Fig. 5b. Our findings reveal that the bubbles (composed of nitrogen molecules) carry no charge, and the charge arises solely from water molecules. Specifically, the water molecules organize themselves in a distinctive double-layer charge structure around the bubbles, primarily due to their preferential orientation at the gas-liquid interface. Remarkably, this double-layer electrostatic charge structure persists even at the horizontal interface, owing to the alignment of the dipole moment of water molecules parallel to the interfacial normal vector. The outer layer's negative charge hinders the merging of neighboring nanobubbles, which precludes the formation of microbubbles, and thus avoids their rupture due to buoyancy. The charge oscillations in the liquid region may be due to the haphazard arrangement of water molecules, but the average charge in the liquid region of nanobubbles at different radii is zero.

According to the description of Henry's law, the solubility of gas in a liquid is related to the partial pressure. The Henry's law gives:

$$P_g = HX \tag{6}$$

Where P_g is the partial pressure of the gas, H is Henry's constant (The Henry's constant for nitrogen is 9.2×10^9 pa at 300k) and X is the solubility. The solubility of a bubble in a liquid can be determined through the application of Henry's law, which predicts the pressure within the bubble at thermodynamic equilibrium, as illustrated in Fig. 4a. The reliability of Henry's law in the context of nanobubbles was confirmed by comparing computed and simulated results, as presented in Table 2. The trends observed in both sets of results were in agreement and fell within the same order of magnitude. Specifically, it was observed that under high pressure, smaller bubbles exhibited increased solubility.

3.4. Brownian motion of nanobubbles

The motion properties of nanobubbles are critical in industrial applications. To observe the Brownian motion of the nanobubbles, we lifted the restriction on the center of mass of the bubbles and performed 2-ns NVE simulations to count the liquid-gas properties of the bubbles as they undergo Brownian motion. Our analysis shows when the nanobubbles achieve a dynamic equilibrium, the diffusion of the contained gases becomes slower. We have further visualized and confirmed the majority of gas molecules are still in the bubble region. We found that over 80 % of the gas molecules are maintained within the nanobubbles which can be attributed to the liquid's saturation (refer to Supplementary Information Figure S5). Therefore, the molecules inside the nanobubbles at steady state can be used to analyze the nanobubble motion. Our results, presented in Fig. 6, demonstrate the Brownian motion of

Table 2
Dissolution of nanobubbles in liquids (molar fraction representation).

Bubble radius	$R = 14$ Å	$R = 18$ Å	$R = 22$ Å
Solubility (Henry's law)	0.0087	0.0071	0.0057
Solubility (Simulation)	0.0063	0.0049	0.0036

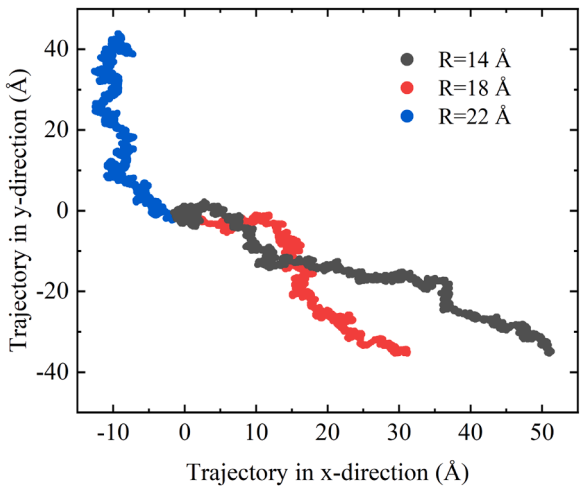

Fig. 6. The Brownian motion trajectory of bubbles with different radius in NVE ensembles for 2 ns. It mainly reflects the displacement of the bubble in the x and y directions.

bubbles with different radii. We observed that smaller bubbles exhibit more intense Brownian motion and travel farther distances over the same period. Furthermore, we found that the Brownian motion rate of nanobubbles is influenced not only by bubble size, but also by the saturation of the surrounding liquid. Both 18 Å and 22 Å bubbles reach supersaturation levels compared to the 14 Å bubbles. As the saturation level increases, the Brownian motion of nanobubbles decreases. The variability in the Brownian motion rates of nanobubbles within liquids is primarily attributed to collisions between liquid and gas molecules, which lead to distinctive levels of motion resistance. In the realm of statistical physics, the friction coefficient is directly linked to the fluctuations of the force exerted on the equilibrium entity. To accurately quantify the resistance encountered during nanobubble motion, we calculated the friction coefficients experienced by individual nanobubbles of various sizes. This calculation was performed using the Green-Kubo integral of the force autocorrelation [54], employing the following mathematical expression:

$$\xi(t) = \frac{1}{3K_B T} \int_0^t \langle F(S) \cdot F(0) \rangle dt \tag{7}$$

where K_B is the Boltzmann constant, T is the temperature at system stability, $\langle F(S) \cdot F(0) \rangle$ is the average of the autocorrelation function of the interaction forces of the liquid and the gas at different time starting points.

The analysis reveals that the nanobubbles with varying radii experience rapid decay within 100 fs, as indicated by their force autocorrelation. Smaller bubbles exhibit a greater amplitude of oscillation, but all eventually stabilize after 600 fs. By applying the average value of the autocorrelation function to Eq. (7), the friction coefficient for nanobubbles of different radii was computed, and the results are presented in Fig. 7a. Notably, larger bubbles exhibit a higher coefficient of friction, with the 22 Å bubble having roughly twice the coefficient of friction as the 14 Å bubble. The Brownian motion of nanobubbles is fundamentally influenced by their gas-liquid interaction. In Fig. 7b, we present the interaction forces and energies of moving bubbles (The detailed calculations are provided in the supplementary information.). Specifically, larger bubbles experience greater gas-liquid interaction and energy (absolute value) during Brownian motion, which impedes their movement. Furthermore, the dissolution and movement of nanobubbles typically happen concurrently. We calculated the forces exerted on distinct gas molecules within these bubbles when immersed in liquid. For bubbles with radii of 14 Å, 18 Å, and 22 Å, the forces on the gas

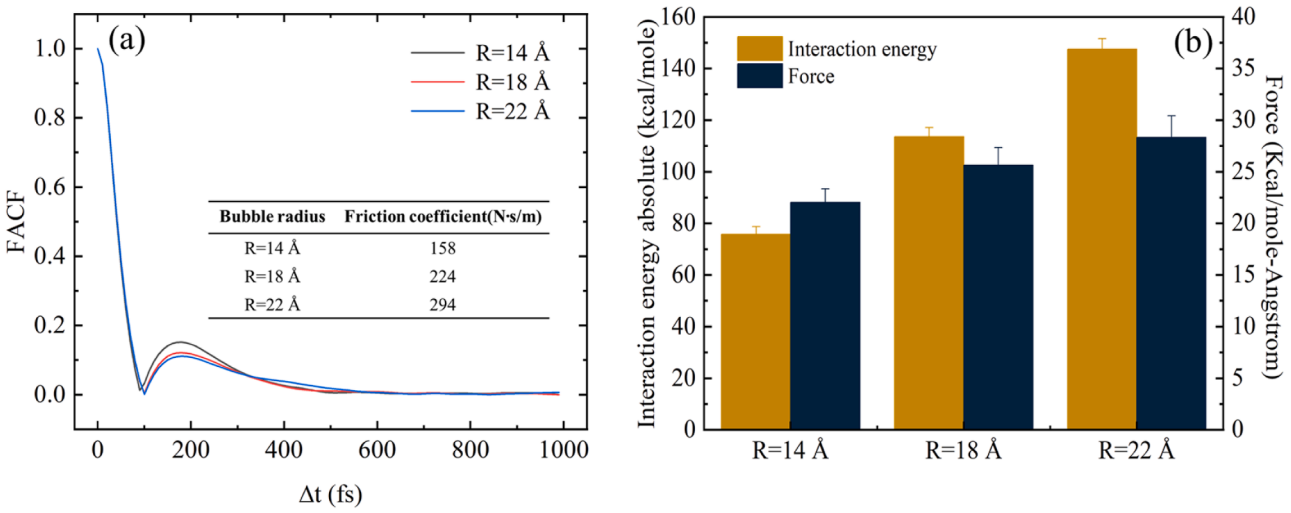

Fig. 7. (a)The normalized autocorrelation functions of force were determined for nanobubbles of varying radii. The corresponding friction coefficient was calculated from the Green-Kubo integral of the force autocorrelations, as shown in the inset table. (b) Interaction forces absolute and energies of moving nanobubbles.

molecules were found to be 0.21, 0.09, and 0.07 (kcal/mol)/Angstrom, respectively. This suggests that gas molecules in smaller bubbles experience greater liquid forces, facilitating their diffusion. These findings align with the Mean Square Displacement (MSD) calculations illustrated in Fig. 3a, which focus on the behavior of bubble molecules.

4. Conclusion

Our study presents a comprehensive investigation into the stability of nanobubbles, employing molecular dynamics simulations and classical bubble stability theory. The results highlight the relationship between different parameters and bubble stability. Specifically, our findings indicate that large nanobubbles possess a longer lifespan and exhibit lower internal pressures compared to their smaller counterparts. For instance, nanobubbles with radii of 14 Å, 18 Å, and 22 Å correspond to pressures of 792 atm, 647 atm, and 518 atm, respectively. This establishes a clear correlation between bubble size and internal pressure. Furthermore, our analysis uncovers distinctive characteristics of smaller bubbles, including a more stretched state and a thicker liquid-gas interface when compared to larger bubbles. Additionally, we conducted a charge distribution calculation for water molecules surrounding the nanobubbles, which revealed the presence of a stable double-layer electrostatic charge structure. To validate our findings, we employed Henry's law to calculate the solubility of nanobubbles, and the results aligned with our simulation outcomes. Additionally, we examined the surface tension of the calculated plane using Young's equation, and found that it correlated well with simulation data. Notably, according to the results derived from Young's equation, the gas density has minimal influence on the surface tension of nanobubbles. Moreover, through calculations of gas-liquid interactions and mean squared displacement analysis, we demonstrate that gas molecules within smaller bubbles experience more pronounced liquid forces and exhibit enhanced diffusion compared to those within larger bubbles. Overall, our findings provide novel insights into the generation of stable nanobubbles for diverse applications. These insights hold significant implications for fields such as materials science and biomedicine, offering exciting prospects for their design and utilization.

Associated content

Correlation potential functions for nitrogen and water; Initial physical model of the bulk bubble; Dissolution curves of the (a) small, (b) medium and (c) large nanobubbles under NPT conditions; Calculation of surface tension at the interface between different gas densities and solids.

CRediT authorship contribution statement

Jiajie Lei: Writing – review & editing, Writing – original draft, Methodology, Formal analysis, Data curation. **Dezhao Huang:** Writing – review & editing, Writing – original draft, Visualization, Supervision, Resources, Project administration, Methodology, Investigation. **Wensheng Zhao:** Resources, Investigation, Conceptualization. **Sheng Liu:** Supervision, Investigation, Conceptualization. **Yanan Yue:** Visualization, Validation, Supervision, Software, Resources, Investigation, Funding acquisition.

Declaration of competing interest

The authors declare that they have no known competing financial interests or personal relationships that could have appeared to influence the work reported in this paper.

Data availability

The data that support the findings of this study are available from the corresponding author upon reasonable request.

Acknowledgments

This work is supported by the National Key R&D Program of China (No. 2023YFE0120200), National Natural Science Foundation of China (No. 52206107, 52076156) and Fundamental Research Funds for the Central Universities (No. 2042023kf0101). The simulations were supported by the Research Computing Center in Wuhan University.

Supplementary materials

Supplementary material associated with this article can be found, in the online version, at doi:10.1016/j.ijheatmasstransfer.2024.125407.

References

[1] ISO 20480-1:2017. fine bubble technology-general principles for usage and measurement of fine bubbles–Part 1: terminology (2017). Available online: https://www.iso.org/standard/68187.

[2] J. Li, A. Xi, H. Qiao, Z. Liu, Ultrasound-mediated diagnostic imaging and advanced treatment with multifunctional micro/nanobubbles, Cancer Lett. 475 (2020) 92–98, https://doi.org/10.1016/j.canlet.2020.01.028.

[3] H. Li, Z. Wu, J. Zhang, X. Sun, F. Duan, J. Yao, M. Sun, J. Zhang, L. Nie, Instant ultrasound-evoked precise nanobubble explosion and deep photodynamic therapy for tumors guided by molecular imaging, ACS Appl. Mater. Interfaces 13 (2021) 21097–21107, https://doi.org/10.1021/acsami.1c05517.

[4] P. Bhandari, X. Wang, J. Irudayaraj, Oxygen nanobubble tracking by light scattering in single cells and tissues, ACS Nano 11 (2017) 2682–2688, https://doi.org/10.1021/acsnano.6b07478.

[5] K.R. Marcelino, L. Ling, S. Wongkiew, H.T. Nhan, K.C. Surendra, T. Shitanaka, H. Lu, S.K. Khanal, Nanobubble technology applications in environmental and agricultural systems: opportunities and challenges, Crit Rev Environ Sci Technol (2022) 1–26, https://doi.org/10.1080/10643389.2022.2136931.

[6] W. Shi, G. Pan, Q. Chen, L. Song, L. Zhu, X. Ji, Hypoxia remediation and methane emission manipulation using surface oxygen nanobubbles, Environ. Sci. Technol. 52 (2018) 8712–8717, https://doi.org/10.1021/acs.est.8b02320.

[7] D. Huang, J. Schiffbauer, E. Lee, T. Luo, Ballistic Brownian motion of supercavitating nanoparticles, Phys. Rev. E 103 (2021) 042104, https://doi.org/10.1103/PhysRevE.103.042104.

[8] E. Lee, D. Huang, T. Luo, Ballistic supercavitating nanoparticles driven by single Gaussian beam optical pushing and pulling forces, Nat. Commun. 11 (2020) 2404, https://doi.org/10.1038/s41467-020-16267-9.

[9] H. Babar, H. Wu, W. Zhang, Investigating the performance of conventional and hydrophobic surface heat sink in managing thermal challenges of high heat generating components, Int J Heat Mass Transf 216 (2023) 124604, https://doi.org/10.1016/j.ijheatmasstransfer.2023.124604.

[10] Y. Tomo, K. Takahashi, T. Nishiyama, T. Ikuta, Y. Takata, Nanobubble nucleation studied using Fresnel fringes in liquid cell electron microscopy, Int J Heat Mass Transf 108 (2017) 1460–1465, https://doi.org/10.1016/j.ijheatmasstransfer.2017.01.013.

[11] D. Huang, T. Zhang, G. Xiong, L. Xu, Z. Qu, E. Lee, T. Luo, Tuning water slip behavior in nanochannels using self-assembled monolayers, ACS Appl. Mater. Interfaces 11 (2019) 32481–32488, https://doi.org/10.1021/acsami.9b09509.

[12] W. Liu, X. Huang, Y. Yue, Tuning thermal transport across monolayer MoS2/Si heterostructure via substrate nanogrooving, Int J Heat Mass Transf 201 (2023) 123673, https://doi.org/10.1016/j.ijheatmasstransfer.2022.123673.

[13] Q. Zhang, R.D. Neal, D. Huang, S. Neretina, E. Lee, T. Luo, Surface Bubble Growth in Plasmonic Nanoparticle Suspension, ACS Appl. Mater. Interfaces (2020) 8.

[14] R. Kimura, H. Teshima, Q.Y. Li, K. Takahashi, Thermally induced mass transfer between nanobubbles and micropancakes, Int J Heat Mass Transf 181 (2021) 122001, https://doi.org/10.1016/j.ijheatmasstransfer.2021.122001.

[15] H. Meng, S. Maruyama, R. Xiang, N. Yang, Thermal conductivity of one-dimensional carbon-boron nitride van der Waals heterostructure: a molecular dynamics study, Int J Heat Mass Transf 180 (2021) 121773, https://doi.org/10.1016/j.ijheatmasstransfer.2021.121773.

[16] H. Meng, D. Ma, X. Yu, L. Zhang, Z. Sun, N. Yang, Thermal conductivity of molybdenum disulfide nanotube from molecular dynamics simulations, Int J Heat Mass Transf 145 (2019) 118719, https://doi.org/10.1016/j.ijheatmasstransfer.2019.118719.

[17] D. Ma, H. Ding, X. Wang, N. Yang, X. Zhang, The unexpected thermal conductivity from graphene disk, carbon nanocone to carbon nanotube, Int J Heat Mass Transf 108 (2017) 940–944, https://doi.org/10.1016/j.ijheatmasstransfer.2016.12.092.

[18] B.H. Tan, H. An, C.D. Ohl, Stability of surface and bulk nanobubbles, Curr Opin Colloid Interface Sci 53 (2021) 101428, https://doi.org/10.1016/j.cocis.2021.101428.

[19] D. Lohse, X. Zhang, Surface nanobubbles and nanodroplets, Rev. Mod. Phys. 87 (2015) 981–1035, https://doi.org/10.1103/RevModPhys.87.981.

[20] D. Lohse, X. Zhang, Pinning and gas oversaturation imply stable single surface nanobubbles, Phys. Rev. E 91 (2015) 031003, https://doi.org/10.1103/PhysRevE.91.031003.

[21] S. Maheshwari, M. Van Der Hoef, X. Zhang, D. Lohse, Stability of surface nanobubbles: a molecular dynamics study, Langmuir 32 (2016) 11116–11122, https://doi.org/10.1021/acs.langmuir.6b00963.

[22] L. Zhou, S. Wang, L. Zhang, J. Hu, Generation and stability of bulk nanobubbles: a review and perspective, Curr Opin Colloid Interface Sci 53 (2021) 101439, https://doi.org/10.1016/j.cocis.2021.101439.

[23] B.H. Tan, H. An, C.D. Ohl, How Bulk Nanobubbles Might Survive, Phys. Rev. Lett. 124 (2020) 134503, https://doi.org/10.1103/PhysRevLett.124.134503.

[24] F. Eklund, M. Alheshibri, J. Swenson, Differentiating bulk nanobubbles from nanodroplets and nanoparticles, Curr Opin Colloid Interface Sci 53 (2021) 101427, https://doi.org/10.1016/j.cocis.2021.101427.

[25] T. Temesgen, T.T. Bui, M. Han, T. Kim, H. Park, Micro and nanobubble technologies as a new horizon for water-treatment techniques: a review, Adv Colloid Interface Sci 246 (2017) 40–51, https://doi.org/10.1016/j.cis.2017.06.011.

[26] E.D. Michailidi, G. Bomis, A. Varoutoglou, G.Z. Kyzas, G. Mitrikas, A. Ch. Mitropoulos, E.K. Efthimiadou, E.P. Favvas, Bulk nanobubbles: production and investigation of their formation/stability mechanism, J Colloid Interface Sci 564 (2020) 371–380, https://doi.org/10.1016/j.jcis.2019.12.093.

[27] N. Nirmalkar, A.W. Pacek, M. Barigou, Interpreting the interfacial and colloidal stability of bulk nanobubbles, Soft Matter 14 (2018) 9643–9656, https://doi.org/10.1039/C8SM01949E.

[28] M.R. Ghaani, P.G. Kusalik, N.J. English, Massive generation of metastable bulk nanobubbles in water by external electric fields, Sci. Adv. 6 (2020) eaaz0094, https://doi.org/10.1126/sciadv.aaz0094.

[29] T. Yildirim, S. Yaparatne, J. Graf, S. Garcia-Segura, O. Apul, Electrostatic forces and higher order curvature terms of Young–Laplace equation on nanobubble stability in water, Npj Clean Water 5 (2022) 18, https://doi.org/10.1038/s41545-022-00163-4.

[30] K. Agarwal, M. Trivedi, N. Nirmalkar, Does salting-out effect nucleate nanobubbles in water: spontaneous nucleation? Ultrason Sonochem 82 (2022) 105860 https://doi.org/10.1016/j.ultsonch.2021.105860.

[31] A.P. Thompson, H.M. Aktulga, R. Berger, D.S. Bolintineanu, W.M. Brown, P. S. Crozier, P.J. in 't Veld, A. Kohlmeyer, S.G. Moore, T.D. Nguyen, R. Shan, M. J. Stevens, J. Tranchida, C. Trott, S.J. Plimpton, LAMMPS - a flexible simulation tool for particle-based materials modeling at the atomic, meso, and continuum scales, Comput Phys Commun 271 (2022) 108171, https://doi.org/10.1016/j.cpc.2021.108171.

[32] A. Stukowski, Visualization and analysis of atomistic simulation data with OVITO–the open visualization tool, Modelling Simul. Mater. Sci. Eng. 18 (2010) 015012, https://doi.org/10.1088/0965-0393/18/1/015012.

[33] Z. Gao, W. Wu, W. Sun, B. Wang, Understanding the stabilization of a bulk nanobubble: a molecular dynamics analysis, Langmuir 37 (2021) 11281–11291, https://doi.org/10.1021/acs.langmuir.1c01796.

[34] E. Bird, E. Smith, Z. Liang, Coalescence characteristics of bulk nanobubbles in water: a molecular dynamics study coupled with theoretical analysis, Phys. Rev. Fluids 6 (2021) 093604, https://doi.org/10.1103/PhysRevFluids.6.093604.

[35] Wang Chun-Lei, Li Zhao-Xia, Li Jing-Yuan, Xiu Peng, Hu Jun, Fang hai-ping, high density gas state at water/graphite interface studied by molecular dynamics simulation, Chinese Physics B 17 (2008) 2646, https://doi.org/10.1088/1674-1056/17/7/049.

[36] P. Mark, L. Nilsson, Structure and dynamics of the TIP3P, SPC, and SPC/E water models at 298K, J. Phys. Chem. A 105 (2001) 9954–9960, https://doi.org/10.1021/jp003020w.

[37] M. Rami Reddy, M. Berkowitz, The dielectric constant of SPC/E water, Chem Phys Lett 155 (1989) 173–176, https://doi.org/10.1016/0009-2614(89)85344-8.

[38] F. Chen, P.E. Smith, Simulated surface tensions of common water models, J. Chem. Phys. 126 (2007) 221101, https://doi.org/10.1063/1.2745718.

[39] R.W. Hockney, J.W. Eastwood, Computer Simulation Using Particles, CRC Press, 2021, https://doi.org/10.1201/9780367806934, 0 ed.

[40] E.J. Maginn, R.A. Messerly, D.J. Carlson, D.R. Roe, J.R. Elliot, Best practices for computing transport properties 1. Self-diffusivity and viscosity from equilibrium molecular dynamics [Article v1.0], LiveCoMS 2 (2020), https://doi.org/10.33011/livecoms.1.1.6324.

[41] S.M. Thompson, K.E. Gubbins, J.P.R.B. Walton, R.A.R. Chantry, J.S. Rowlinson, A molecular dynamics study of liquid drops, J Chem Phys 81 (1984) 530–542, https://doi.org/10.1063/1.447358.

[42] P.R. Ten Wolde, D. Frenkel, Computer simulation study of gas–liquid nucleation in a lennard-jones system, J Chem Phys 109 (1998) 9901–9918, https://doi.org/10.1063/1.477658.

[43] M. Zhang, Y. Tu, H. Fang, Concentration of nitrogen molecules needed by nitrogen nanobubbles existing in bulk water, Appl. Math. Mech.-Engl. Ed. 34 (2013) 1433–1438, https://doi.org/10.1007/s10483-013-1757-x.

[44] P.S. Epstein, M.S. Plesset, On the stability of gas bubbles in liquid-gas solutions, J. Chem. Phys. 18 (1950) 1505–1509, https://doi.org/10.1063/1.1747520.

[45] M. Feng, X. Ma, Z. Zhang, K.H. Luo, C. Sun, X. Xu, How sodium chloride extends lifetime of bulk nanobubbles in water, Soft Matter 18 (2022) 2968–2978, https://doi.org/10.1039/D2SM00181K.

[46] S.N. Hong, S.H. Choe, U.G. Jong, M.S. Pak, C.J. Yu, The maximum interbubble distance in relation to the radius of spherical stable nanobubble in liquid water: a molecular dynamics study, Fluid Phase Equilib 487 (2019) 45–51, https://doi.org/10.1016/j.fluid.2019.01.014.

[47] X. Wang, P. Li, R. Ning, R. Ratul, X. Zhang, J. Ma, Mechanisms on stability of bulk nanobubble and relevant applications: a review, J Clean Prod 426 (2023) 139153, https://doi.org/10.1016/j.jclepro.2023.139153.

[48] T. Yamamoto, S. Ohnishi, Molecular dynamics study on helium nanobubbles in water, Phys. Chem. Chem. Phys. 13 (2011) 16142, https://doi.org/10.1039/c1cp22018g.

[49] R. Zhang, Y. Gao, L. Chen, G. Ge, Nanobubble boundary layer thickness quantified by solvent relaxation NMR, J Colloid Interface Sci 609 (2022) 637–644, https://doi.org/10.1016/j.jcis.2021.11.072.

[50] Z. Pan, W. Liu, L. Yu, Z. Xie, Q. Sun, P. Zhao, D. Chen, W. Fang, B. Liu, Resonance-induced reduction of interfacial tension of water–methane and improvement of methane solubility in water, Langmuir 38 (2022) 13594–13601, https://doi.org/10.1021/acs.langmuir.2c02392.

[51] I. Prigogine, P. Debye (Eds.), Frontmatter, in: Advances in Chemical Physics, 1st ed., Wiley, 1957 https://doi.org/10.1002/9780470143476.fmatter.

[52] Y. Sun, G. Xie, Y. Peng, W. Xia, J. Sha, Stability theories of nanobubbles at solid–liquid interface: a review, Colloids and Surfaces A: Physicochemical and Engineering Aspects 495 (2016) 176–186, https://doi.org/10.1016/j.colsurfa.2016.01.050.

[53] H. Teshima, H. Kusudo, C. Bistafa, Y. Yamaguchi, Quantifying interfacial tensions of surface nanobubbles: how far can Young's equation explain? Nanoscale 14 (2022) 2446–2455, https://doi.org/10.1039/D1NR07428H.

[54] L. Bocquet, J.P. Hansen, J. Piasecki, On the Brownian motion of a massive sphere suspended in a hard-sphere fluid. II. Molecular dynamics estimates of the friction coefficient, J Stat Phys 76 (1994) 527–548, https://doi.org/10.1007/BF02188674.